



Wireless electrical stimulation at the nanoscale interface induces tumor vascular normalization

Changhao Li^{a,1}, Cairong Xiao^{a,1}, Lizhen Zhan^b, Zhekun Zhang^a, Jun Xing^b, Jinxia Zhai^a, Zhengnan Zhou^a, Guoxin Tan^d, Jinhua Piao^b, Yahong Zhou^c, Suijian Qi^{b,*}, Zhengao Wang^{a,e,**}, Peng Yu^{a,e,***}, Chengyun Ning^{a,e}

^a School of Material Science and Engineering, National Engineering Research Center for Tissue Restoration and Reconstruction, Metallic Materials Surface Functionalization Engineering Research Center of Guangdong Province, South China University of Technology, Guangzhou, 510641, China

^b School of Food Science and Engineering, South China University of Technology, Guangzhou, 510641, China

^c CAS Key Laboratory of Bio-inspired Materials and Interfacial Science, Technical Institute of Physics and Chemistry, Chinese Academy of Science, Beijing, 100190, China

^d School of Chemical Engineering and Light Industry, Guangdong University of Technology, Guangzhou, 510006, China

^e China-Singapore International Joint Research Institute, Guangzhou, 511365, China

ARTICLE INFO

Keywords:

Calcium distribution
Mechano-electrical conversion
Piezoelectric barium titanate
Tumor vascular normalization
Wireless electrical stimulation

ABSTRACT

Pathological angiogenesis frequently occurs in tumor tissue, limiting the efficiency of chemotherapeutic drug delivery and accelerating tumor progression. However, traditional vascular normalization strategies are not fully effective and limited by the development of resistance. Herein, inspired by the intervention of endogenous bioelectricity in vessel formation, we propose a wireless electrical stimulation therapeutic strategy, capable of breaking bioelectric homeostasis within cells, to achieve tumor vascular normalization. Polarized barium titanate nanoparticles with high mechano-electrical conversion performance were developed, which could generate pulsed open-circuit voltage under low-intensity pulsed ultrasound. We demonstrated that wireless electrical stimulation significantly inhibited endothelial cell migration and differentiation *in vitro*. Interestingly, we found that the angiogenesis-related eNOS/NO pathway was inhibited, which could be attributed to the destruction of the intracellular calcium ion gradient by wireless electrical stimulation. *In vivo* tumor-bearing mouse model indicated that wireless electrical stimulation normalized tumor vasculature by optimizing vascular structure, enhancing blood perfusion, reducing vascular leakage, and restoring local oxygenation. Ultimately, the anti-tumor efficacy of combination treatment was 1.8 times that of the single chemotherapeutic drug doxorubicin group. This work provides a wireless electrical stimulation strategy based on the mechano-electrical conversion performance of piezoelectric nanoparticles, which is expected to achieve safe and effective clinical adjuvant treatment of malignant tumors.

1. Introduction

Malignant tumor growth and progression are promoted by pathological angiogenesis, characterized by blood vessels that are defective structurally and functionally. The resultant abnormal tumor vasculature will lead to poor blood perfusion and local tissue hypoxia, greatly

hindering the delivery and efficacy of chemotherapeutic drugs [1,2]. In recent years, normalization of tumor blood vessels induced by anti-angiogenic drugs has been viewed as a new strategy for treating malignant tumors [3,4]. However, the drawbacks of anti-angiogenic drugs, shown by many preclinical and clinical studies include transient effects, drug resistance, and potential cytotoxicity [5–7].

Peer review under responsibility of KeAi Communications Co., Ltd.

* Corresponding author. School of Food Science and Engineering, South China University of Technology, Guangzhou, 510640, China.

** Corresponding author. School of Material Science and Engineering, South China University of Technology, Guangzhou, 510640, China.

*** Corresponding author. School of Material Science and Engineering, South China University of Technology, Guangzhou, 510640, China.

E-mail addresses: fesuijianqi@scut.edu.cn (S. Qi), zhengao@scut.edu.cn (Z. Wang), imyup@scut.edu.cn (P. Yu).

¹ These authors contributed equally to this work.

<https://doi.org/10.1016/j.bioactmat.2022.03.027>

Received 21 January 2022; Received in revised form 15 March 2022; Accepted 16 March 2022

2452-199X/© 2022 The Authors. Publishing services by Elsevier B.V. on behalf of KeAi Communications Co. Ltd. This is an open access article under the CC BY-NC-ND license (<http://creativecommons.org/licenses/by-nc-nd/4.0/>).

Moreover, the normalization process required strict adherence to tedious dose and time regimes, which largely reduce the flexibility of subsequent chemotherapeutic drug treatments [8,9]. Thus, there remains an urgent need to explore a clinically effective method for tumor vascular normalization from a different perspective.

Bioelectricity is a basic attribute of living organisms and is necessary for regulating the vascular network during embryonic development, tissue repair, and tumor progression [10–12]. Thus, regulating the bioelectric balance of blood vessels might be an alternative strategy for normalizing tumor vasculature. In fact, it has been discovered that exogenous electrical stimulation could interfere with the electric microenvironment of the cell, triggering a series of unique biological effects, such as reactive oxygen generation, calcium fluctuation, and actin reorganization [13–15]. Moreover, exogenous electrical stimulation was demonstrated to reduce the density of tumor vasculature and downregulate the expression of angiogenesis-related factors [16–18]. However, despite their advantages as an alternative drug-free and non-thermal technique, the invasiveness of electrode placement, the possibility of electric breakdown, and the unachievable cell-scale treatment remained major obstacles for the clinical application of this approach [19–21]. In view of this, the development of a non-invasive, wireless electrical stimulation strategy might break through the existing bottleneck and inspire further exploration of approaches to achieve tumor vascular normalization.

Piezoelectric materials have non-centrosymmetric crystalline structures, which could exhibit unique mechano-electrical behavior in response to external forces (e.g., compressions, vibrations, sounds), providing a potential non-invasive electrical stimulation tool. Piezoelectric nanoparticles are particularly beneficial because of their unique zero-dimensional structure, precisely tunable polarization properties, high spatial specificity and the ability to be phagocytosed into cells for intracellular action in a drug-like manner [22–24]. In this work, tetragonal polarized barium titanate (P-BTO) piezoelectric

nanoparticles with high mechano-electrical conversion performance were developed for tumor vascular normalization. Combined with the low-intensity pulsed ultrasound (LIPUS) loading, the P-BTO nanoparticles exert wireless electrical stimulation at the nanoscale interface through mechano-electrical conversion to inhibit endothelial cell migration and differentiation. *In vivo* animal experiments were carried out to study the effect on tumor vasculature and to explore the subsequent combined treatment effect with chemotherapeutic drug doxorubicin (DOX). The angiogenesis-related endothelial nitric oxide synthase (eNOS) expression, nitric oxide production, as well as intracellular calcium ions ($[Ca^{2+}]_i$) distribution was analyzed to reveal the underlying mechanism of wireless electrical stimulation on tumor vessel normalization. This work presents a wireless electrical stimulation strategy via mechano-electrical conversion at the nanoscale interface to normalize tumor blood vessels, which has broad application prospects in the clinical auxiliary treatment of malignant tumors.

2. Results and discussion

2.1. Characterizing the wireless electrical cues at the nanoscale interface

In order to realize wireless electrical stimulation at the nanoscale interface, we constructed mechano-electrical responsive barium titanate (BTO) nanoparticles via a solvothermal process (Fig. S1). Subsequently, we polarized the untreated BTO (U-BTO) nanoparticles by an external electric polarization device. After the external polarization field was removed, the regularized electric domains arrangements continued to contribute to the improvement of piezoelectric properties [25]. Transmission electron microscopic (TEM) images and scanning electron microscopic (SEM) images showed that P-BTO nanoparticles exhibited regular morphology and a homogeneous size, with good dispersibility (Fig. 1a and Fig. S2a). High-resolution transmission electron microscopic (HRTEM) images suggested that P-BTO nanoparticles produced

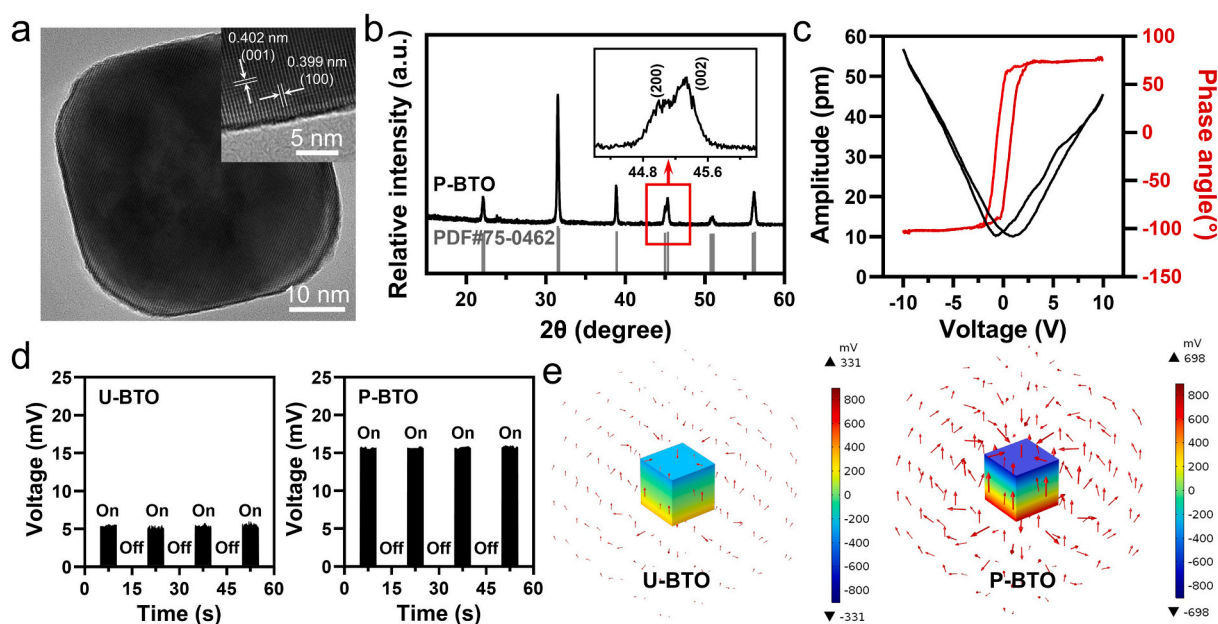


Fig. 1. Microstructure and mechano-electrical properties of P-BTO nanoparticles. (a) TEM images & HRTEM images (insert) of P-BTO nanoparticles. The lattice spacings were 0.399 and 0.402 nm for the (100) and (001) planes of the tetragonal phase, respectively. (b) XRD patterns of P-BTO nanoparticles and the enlarged (002) and (200) peaks around $2\theta = 45^\circ$ (insert). Standard JCPDS of PDF#75-0462 corresponds to the tetragonal $BaTiO_3$ structure. (c) PFM amplitude curve and phase curve of P-BTO nanoparticles when applying a ramp voltage from -10 to 10 V at room temperature. (d) Digital source meter records of the open-circuit voltages of U-BTO and P-BTO nanoparticles under the same LIPUS (1 MHz, 1.0 W/cm²). The x-axis refers to the time axis of signal recording. The on/off sign represents the time period of LIPUS on/off. (e) COMSOL simulation of piezoelectric potential distribution in U-BTO and P-BTO nanoparticles under the same pressure. The red arrow represents the vector of the spatial electric field formed by the piezoelectric potential difference between the upper and lower surfaces under the action of the external force field. These results indicated that the tetragonal phase P-BTO nanoparticles exhibited desirable piezoelectricity, which could generate wireless electrical stimulation with high efficiency.

clear lattice fringes and demonstrated good crystallinity (Fig. 1a, inset). The lattice spacing was 0.399 and 0.402 nm, corresponding to the (100) and (001) planes of the tetragonal phase, respectively [26]. Energy dispersive spectrometry (EDS) indicated that the Ba, Ti and O elements were uniformly distributed in nanoparticles (Fig. S2b). The average particle diameter of P-BTO nanoparticles, as determined by dynamic light scattering (DLS), was 120.70 ± 41.48 nm, which was consistent with the data from SEM (Fig. S2c). The X-ray diffraction (XRD) results showed the asymmetric peaks were around $2\theta = 45^\circ$, corresponding to separated (002) and (200) peaks, which were consistent with the standard tetragonal BTO structure (JCPDS, PDF#75-0462) (Fig. 1b) [27,28]. In addition, piezoelectric response force microscopy (PFM) was used to characterize their piezoelectric response (Fig. 1c). A typical butterfly amplitude loop and ca. 180° phase switching were recorded by applying a ramp voltage from -10 to 10 V, revealing ferroelectric polarization switching under the external electric field and demonstrating the desirable piezoelectric response of P-BTO nanoparticles [29]. These data confirmed the successful preparation of tetragonal P-BTO nanoparticles, and their desirable piezoelectric properties were expected to realize the intelligent conversion of mechanical signals into electrical signals.

To achieve wireless electrical stimulation based on BTO nanoparticles, we chose to use LIPUS as an external mechanical source. Due to its non-invasiveness and high tissue-penetrating capability, LIPUS can safely and efficiently manipulate the electrical signal output of piezoelectric nanoparticles in remote modality [30,31]. To compare the mechano-electrical responsivity of U-BTO and P-BTO nanoparticles directly, we tested the electrical signal output under LIPUS loading with different power (1 MHz, 0.25–2.25 W/cm²) using a digital source meter. Both U-BTO nanoparticles and P-BTO nanoparticles exhibited a continuous pulse signal (Fig. 1d, Fig. S3). Combining the biosafety issue together with electrical signal output, we selected LIPUS with parameters of 1 MHz and 1.0 W/cm² for follow-up research [24,30]. Strikingly, P-BTO nanoparticles recorded a two-fold increase in open-circuit voltage (ca. 15 mV) under the same LIPUS conditions (1 MHz, 1.0 W/cm²) than that of U-BTO nanoparticles, which indicated that polarization enhanced piezoelectricity by regularizing the arrangement of electric domains. Subsequently, the mechano-electrical conversion process of U-BTO and P-BTO nanoparticles under pressure was simulated through COMSOL finite element modeling. When the BTO model cube with a side length of 120 nm was placed in an external mechanical field of 10^8 Pa, the upper and lower surfaces showed piezoelectric potentials of different polarities (Fig. 1e). Consistent with the measurement results of the digital source meter, P-BTO nanoparticles presented a higher potential difference at the surface than that of U-BTO nanoparticles, indicating an optimized piezoelectric output. These data indicated that P-BTO nanoparticles have a high mechano-electrical conversion efficiency, making them more potent for generating wireless, non-invasive and cell-scale electrical stimulations to cells and tissues.

2.2. Wireless electrical stimulation inhibits endothelial cell migration and angiogenesis *in vitro*

To explore the initial biological performance of wireless electrical stimulation, the human umbilical vein endothelial cells (HUVECs) were co-cultured with piezoelectric nanoparticles at LIPUS loading state. The experimental and control groups were set as blank, blank + LIPUS, U-BTO, U-BTO + LIPUS, P-BTO and P-BTO + LIPUS. First, cell counting kit-8 (CCK-8) assay was conducted to evaluate the cytotoxicity. The results of the blank group and blank + LIPUS group jointly confirmed the biosafety of LIPUS under current parameters, which allowed exploration of the biological effects of wireless electrical stimulation per se (Fig. S4). Irrespective of whether LIPUS loading was used, none of the BTO treatment groups produced toxicity to the cells, even at a concentration as high as 200 µg/mL, indicating that both nanoparticles and wireless electrical stimulation showed good biocompatibility. In the

subsequent *in vitro* experiment, the nanoparticles concentration was set at 100 µg/mL. To evaluate the potential effects of wireless electrical stimulation on angiogenesis, two-dimensional Matrigel cultures were used to characterize tube formation. Compared with the blank group, the blank + LIPUS group, U-BTO group, and P-BTO group presented similar tight tubular structures at 24 h, showing that LIPUS and BTO nanoparticles had no negative effect on the formation of tube-like structures (Fig. 2a). In contrast, the U-BTO + LIPUS group showed minor decreases in the number of tube branches and tube lengths. Interestingly, we observed that the P-BTO + LIPUS group failed to form the typical tube blood vessel network. Statistical analysis showed that tube formation was inhibited by 70%, which indicated that enhanced wireless electrical stimulation had a better anti-angiogenesis effect (Fig. 2b). Based on the critical role of endothelial migration in cell recruitment and remodeling into tubular structures, the effect of wireless electrical stimulation on cell migration was further measured through the scratch wound assay [32,33]. Significant closure of the scratch area was detected in the blank group, the blank + LIPUS group, U-BTO group and P-BTO group, showing good cell migration ability (Fig. 2c). In contrast, the degrees of cell migration were significantly reduced in the U-BTO + LIPUS group and P-BTO + LIPUS group. The migration index of the P-BTO + LIPUS group dropped by nearly 60% compared to the blank group, indicating that enhanced wireless electrical stimulation showed a stronger ability to inhibit cell migration (Fig. 2d). Our results demonstrated that wireless electrical stimulation could achieve *in vitro* anti-angiogenic activity similar to that of nutlin-loaded functionalized piezoelectric nanoparticles [34]. Since cell migration is closely related to cytoskeleton, the effect of wireless electrical stimulation on f-actin assembly was further studied [35]. It could be observed that the cells in the U-BTO + LIPUS group and P-BTO + LIPUS group did not show obvious front-end protrusion, and the formation of lamellar pseudopodia was also greatly reduced, indicating that the inhibition of cell migration by wireless electrical stimulation was related to the reduced cytoskeleton rearrangement (Fig. S5) [36]. Considering that angiogenesis is regulated by multiple growth factors and cytokines, the expression of several important angiogenesis-related genes was examined [37]. In the U-BTO + LIPUS group and P-BTO + LIPUS group, the expression of *VEGF*, *FGF2*, *TGFβ1* and *NOS3* was downregulated, with the latter showing the strongest regulatory effect (Fig. 2e). As a downstream component of angiogenic signal transduction, endothelial nitric oxide synthase (eNOS) has been shown to mediate secretion of vasoactive factors via production of nitric oxide (NO) [38,39]. To reveal the association between wireless electrical stimulation and the eNOS/NO pathway, we then used the fluorescent dye DAF-FM to assess the level of intracellular NO. Strikingly, the intracellular expression of NO was significantly downregulated only in the U-BTO + LIPUS and P-BTO + LIPUS groups, which was consistent with the decrease in the relevant gene expression (Fig. 2f and g). These data indicated that wireless electrical stimulation tended to inhibit the recruitment of endothelial cells to form blood vessels by downregulating the eNOS/NO pathway.

2.3. Wireless electrical stimulation disrupts intracellular calcium ion distribution required for endothelial function

Recent studies have suggested that locally active intracellular calcium ions ($[Ca^{2+}]_i$) act on enzymes such as NO synthase and phospholipase to regulate the secretion of vasoactive factors [40–42]. The influence of exogenous electrical stimulation on basic cell activities, such as migration and alignment, has also been proven to be closely related to the dynamic adjustment of $[Ca^{2+}]_i$ [15,43]. To explore the potential anti-angiogenesis mechanism of wireless electrical stimulation, we used the fluorescent probe Fluo-4AM to monitor changes in $[Ca^{2+}]_i$ in HUVECs. We found that, before LIPUS treatment, cells in all groups presented locally enriched $[Ca^{2+}]_i$ signals, which is required for normal cell activity (Fig. 3a). Within 45s after LIPUS treatment, the

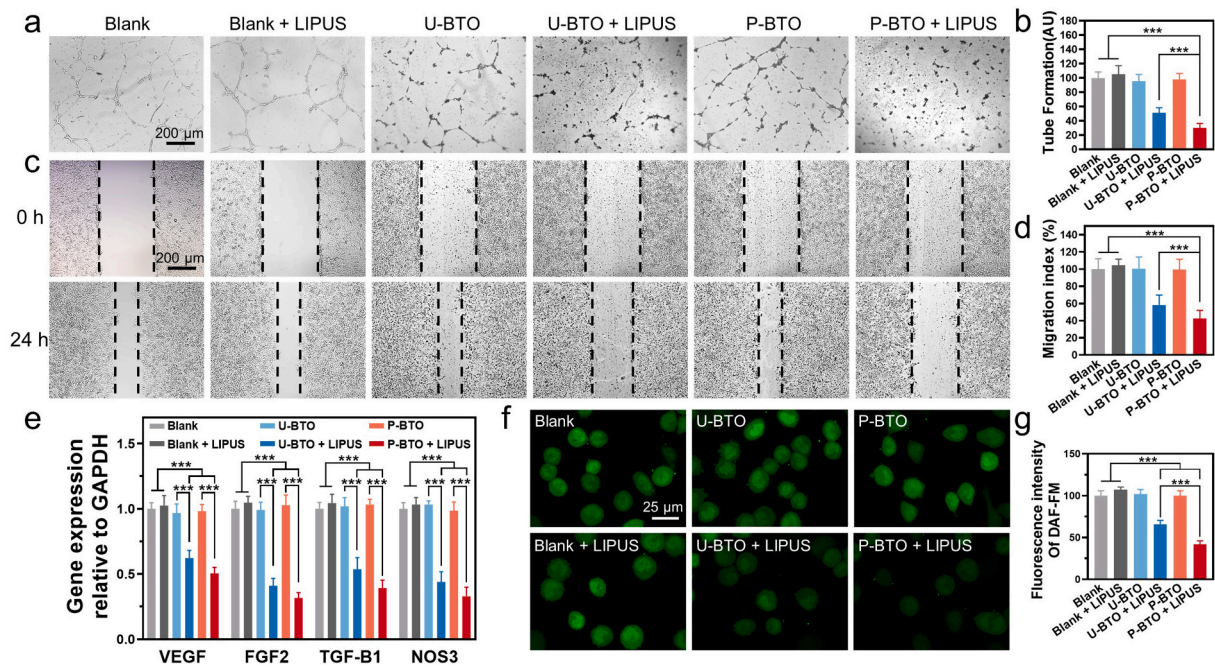


Fig. 2. Effect of wireless electrical stimulation on HUVEC behavior *in vitro*. (a, b) Tube formation assay and quantitative analysis. Data are mean \pm s.d. of biological replicates ($n = 4$). (c, d) Representative migration images and migration index statistics of HUVECs at 0 and 24 h. Data are mean \pm s.d. of biological replicates ($n = 4$). (e) Expression of the angiogenesis-related genes in HUVECs after 48 h. Data are mean \pm s.d. of biological replicates ($n = 6$). (f, g) Intracellular NO staining and quantitative analysis. * $p < 0.05$, ** $p < 0.01$ or *** $p < 0.001$. Enhanced wireless electrical stimulation generated by P-BTO nanoparticles under LIPUS significantly inhibited the recruitment of endothelial cells into blood vessels by downregulating the eNOS/NO pathway.

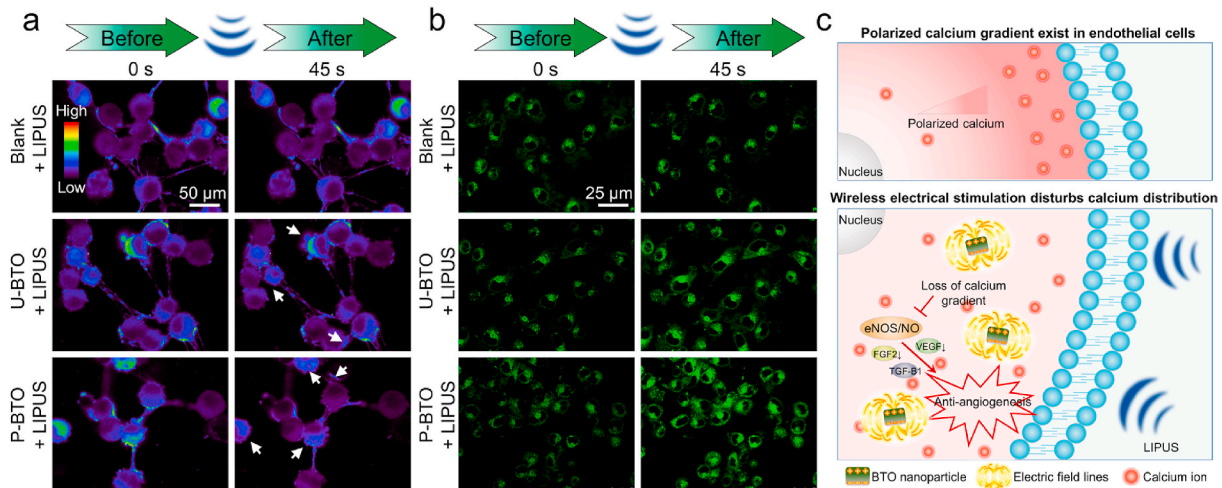


Fig. 3. Effect of wireless electrical stimulation on bioelectric homeostasis of HUVECs. (a) $[Ca^{2+}]_i$ imaging in different groups before and after LIPUS loading. Pseudocolor is used for better identification of concentration gradients. (b) Cell membrane potential imaging of different groups before and after LIPUS loading. (c) Schematic diagram of BTO nanoparticles regulating angiogenesis under LIPUS loading. Wireless electrical stimulation disturbs the original $[Ca^{2+}]_i$ gradient, thereby inhibiting the eNOS/NO pathway and downregulating the secretion of angiogenesis-related factors, which ultimately limits the differentiation of blood vessels. Enhanced wireless electrical stimulation generated by P-BTO nanoparticles could destroy the original $[Ca^{2+}]_i$ gradient to the greatest extent.

distribution of $[Ca^{2+}]_i$ in the blank + LIPUS group did not change significantly, indicating that LIPUS had no regulatory effect on $[Ca^{2+}]_i$. However, after LIPUS treatment, the local distribution of $[Ca^{2+}]_i$ weakened in the U-BTO + LIPUS and P-BTO + LIPUS groups, showing a dependence on the intensity of wireless electrical stimulation. Statistical analysis showed that the intensity of $[Ca^{2+}]_i$ in the U-BTO + LIPUS and P-BTO + LIPUS groups decreased by 15% and 26% after LIPUS treatment, respectively (Fig. S6a). Among them, the local high $[Ca^{2+}]_i$ microregions in the P-BTO + LIPUS group were almost eliminated at 45s after LIPUS treatment, and the original polarized $[Ca^{2+}]_i$ gradient was

disrupted, indicating that wireless electrical stimulation disrupted the original $[Ca^{2+}]_i$ distribution in the cells. Past research has shown that $[Ca^{2+}]_i$ displayed a rear-to-front gradient when the cell continued to move in one direction [44]. In addition, the locally active $[Ca^{2+}]_i$ was also closely related to a series of biological behaviors, such as vascular development and osteogenesis differentiation [45,46]. Under LIPUS loading, U-BTO/P-BTO nanoparticles produced periodic electrical signals, forcing the charged $[Ca^{2+}]_i$ to migrate dynamically along the direction of the electric field. Finally, the distribution of $[Ca^{2+}]_i$ changed from order to disorder, and the local aggregation was weakened, which

in turn affected the subsequent migration and angiogenesis of endothelial cells. To verify the effects of wireless electrical stimulation on the electric microenvironment further, we used the lipophilic anionic fluorescent dye DiBAC4(3) to detect changes in cell membrane potential. When DiBAC4(3) enters the cell, it causes an increase in membrane potential, and a state of depolarization in the cell [47]. Compared with the blank group, no obvious changes in cell membrane potential were observed in the blank + LIPUS group, U-BTO group, or P-BTO group, indicating that LIPUS or BTO nanoparticles alone were insufficient to regulate the electrophysiological activities of cells. However, in both the U-BTO + LIPUS group and P-BTO + LIPUS group, cell membrane potential depolarization occurred (Fig. 3b). Statistical analysis showed that the intensity of membrane potential in the U-BTO + LIPUS and P-BTO + LIPUS groups increased by 44% and 86% after LIPUS treatment respectively (Fig. S6b), which further confirmed that bioelectric homeostasis within cells was broken by wireless electrical stimulation. To determine whether the wireless electrical stimulation at the nanoscale interface can be accurately applied to single cells, we explored the endocytosis of green fluorescent dye (FITC)-labeled nanoparticles in intracellular uptake experiments. At different time-points (0, 3, and 6 h), both U-BTO and P-BTO nanoparticles were easily endocytosed into HUVECs, which was conducive to achieving more effective intracellular electrical stimulation under external LIPUS loading (Fig. S7). Previous experiments have shown that the activation of many downstream effector proteins related to angiogenesis was dependent on locally enriched $[Ca^{2+}]_i$ [48–50]. Therefore, based on the above results, it was plausible that wireless electrical stimulation generated by BTO nanoparticles at LIPUS loading may inhibit angiogenic behaviors by affecting the polarity distribution of $[Ca^{2+}]_i$ (Fig. 3c). In response to extracellular LIPUS, the endocytosed BTO nanoparticles could be activated to generate wireless electrical stimulation, causing damage to the original $[Ca^{2+}]_i$ gradient within the cells. This subsequently inhibited the

activity of the eNOS/NO pathway, thereby downregulating the secretion of angiogenesis-related factors, and ultimately restricting angiogenesis. The enhanced wireless electrical stimulation generated by P-BTO nanoparticles could produce stronger intracellular interference effects than that of U-BTO nanoparticles.

2.4. Wireless electrical stimulation facilitates tumor vascular normalization *in vivo*

To investigate the effects of wireless electrical stimulation on promoting tumor vascular normalization, the A375 melanoma mouse model was established *in vivo*. Intratumoral nanoparticle injection (2.5 mg/kg) and LIPUS treatment (1 MHz, 1.0 W/cm², 10 min) were performed every other day for three times in total. To assess tumor vascular morphology, we double-stained tumor tissue sections to detect CD31 (red) for endothelial cells and α -SMA (green) for pericytes [51,52]. The blank group, the blank + LIPUS group, U-BTO group and P-BTO group all showed a typical tumor vasculature system with chaotic and disorganized blood vessels and insufficient pericyte coverage (Fig. 4a). Remarkably, compared with the blank group, the U-BTO + LIPUS group and P-BTO + LIPUS group decreased tumor vessel density to 10% and 7%, respectively, while increasing the pericyte coverage to 44% and 68% respectively (Fig. 4d). Compared with the U-BTO + LIPUS group, the P-BTO + LIPUS group displayed better vascular treatment effects, the vascular morphology appeared more homogeneous and organized, which indicated that enhanced wireless electrical stimulation could induce a more mature tumor vascular network. To evaluate whether wireless electrical stimulation simultaneously affected vascular function when improving tumor vascular morphology, fluorescein-labeled TRITC-dextran (red) and FITC-lectin (green) were used to examine vascular permeability and perfusion, respectively [53,54]. The U-BTO + LIPUS and P-BTO + LIPUS groups exhibited decreased dextran

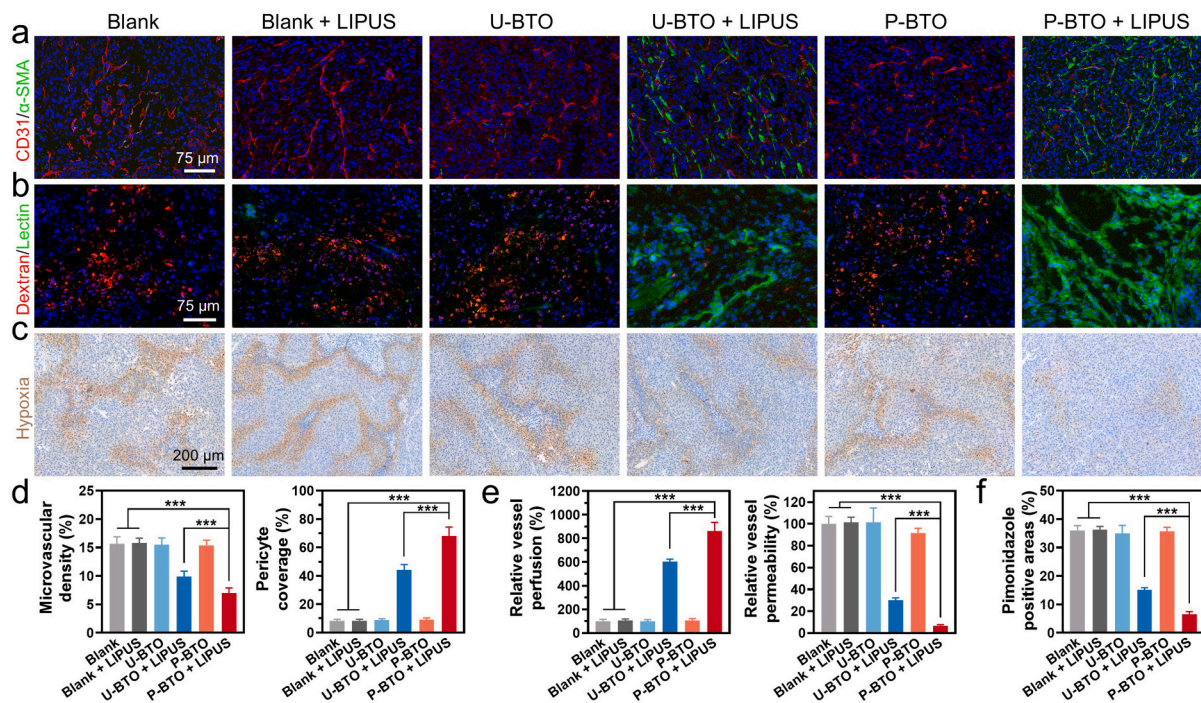


Fig. 4. Effect of wireless electrical stimulation on tumor vascular normalization *in vivo*. (a) Representative images of microvascular morphology. Endothelial cells and pericytes were visualized by CD31 (red) and α -SMA (green). (b) Vessel permeability and perfusion were characterized by injection of TRITC-dextran (red) and FITC-lectin (green). (c) Pimonidazole (brown) staining showed local hypoxia. Data are mean \pm s.d. of biological replicates ($n = 4$). (d) Statistical analysis of microvascular density and pericyte coverage. Data are mean \pm s.d. of biological replicates ($n = 4$). (e) Statistical analysis of vessel perfusion and permeability. Data are mean \pm s.d. of biological replicates ($n = 4$). (f) Statistical analysis of pimonidazole positive areas. Data are mean \pm s.d. of biological replicates ($n = 4$). * $p < 0.05$, ** $p < 0.01$ or *** $p < 0.001$. Enhanced wireless electrical stimulation generated by P-BTO nanoparticles under LIPUS can significantly improve vascular morphology, enhance blood perfusion, reduce vascular leakage, restore local oxygenation, and achieve normalization of tumor vascular structure and function.

permeability and increased lectin perfusion (Fig. 4b). Among them, the P-BTO + LIPUS group showed the least vascular leakage (6% of blank) and the strongest blood perfusion (861% of blank), suggesting that enhanced wireless electrical stimulation helps to improve vascular functionality (Fig. 4e). While no obvious changes in vascular function could be observed in the blank + LIPUS, U-BTO, and P-BTO groups. Considering that tumor oxygenation is another key indicator of tumor vascular normalization, we further analyzed local hypoxia caused by immature vasculature using the hypoxia marker pimonidazole [55,56]. For tumors in the blank group, blank + LIPUS group, U-BTO group, and P-BTO group, strong hypoxia signals were observed (Fig. 4c). Tumors in mice in both the U-BTO + LIPUS group and P-BTO + LIPUS group showed markedly reduced hypoxia signals. Statistical analysis showed that, compared with the blank group (36%), the P-BTO + LIPUS group (7%) had a significantly smaller pimonidazole-positive area, suggesting that the hypoxic tumor environment was greatly improved by the enhanced wireless electrical stimulation (Fig. 4f). Together, these data indicated that wireless electrical stimulation generated by the combination of BTO piezoelectric nanoparticles and LIPUS significantly improved the structure and function of tumor vessels. P-BTO nanoparticles could induce tumor vascular normalization more potently, given the enhanced wireless electrical stimulation conferred by high mechano-electrical conversion efficiency.

2.5. Wireless electrical stimulation induces tumor vascular normalization to potentiate the anti-tumor efficacy of doxorubicin

Encouraged by the effective normalization of tumor blood vessels after wireless electrical stimulation treatment, we further evaluated the anti-tumor efficacy of P-BTO nanoparticles in combination with the

chemotherapy drug DOX [57]. Tumor-bearing mice were divided randomly into eight groups: blank (saline), blank + LIPUS, P-BTO, P-BTO + LIPUS, DOX, DOX + LIPUS, P-BTO + DOX, and P-BTO + DOX + LIPUS. As shown in Fig. 5a, intratumoral nanoparticle injection (2.5 mg/kg) and LIPUS treatment (1 MHz, 1.0 W/cm², 10 min) were administered on the first, third and fifth days. An additional equivalent dose (3.0 mg/kg) of DOX formulation was intravenously administered on the second and fourth days. As expected, after combination therapy, mice in the P-BTO + DOX + LIPUS group showed the most significant tumor growth inhibition effect, which appeared to be markedly better than that achieved with DOX alone (Fig. 5b–d). The tumor volume curves indicated that after day 7, the tumor growth rate of the blank, blank + LIPUS, P-BTO, P-BTO + LIPUS, DOX, DOX + LIPUS and P-BTO + DOX groups accelerated, indicating that single P-BTO nanoparticles, DOX, or wireless electrical stimulation treatment were insufficient to inhibit the growth of tumors. Strikingly, the P-BTO + DOX + LIPUS group showed slightly slowing of tumor growth and exhibited a more significant reduction in growth on day 11, indicating that vascular normalization induced by wireless electrical stimulation greatly enhanced the anti-tumor effect of DOX. The tumor weight, measured on the last day, also confirmed the above results. In the P-BTO + DOX + LIPUS group, the tumor weight was decreased by 86% as compared with the blank group and by 73% as compared with the DOX group. During the treatment period of up to 13 days, the body weight of mice in the eight groups showed no significant difference, suggesting that formulations were not significantly toxic (Fig. 5e). When the mice were sacrificed, the resected tumors were processed for pathological analysis (Fig. 5f, Fig. S8). H&E staining results showed that the combined treatment group demonstrated obvious damage to tumor cells, such as increased intercellular space, extensive nuclear contraction and

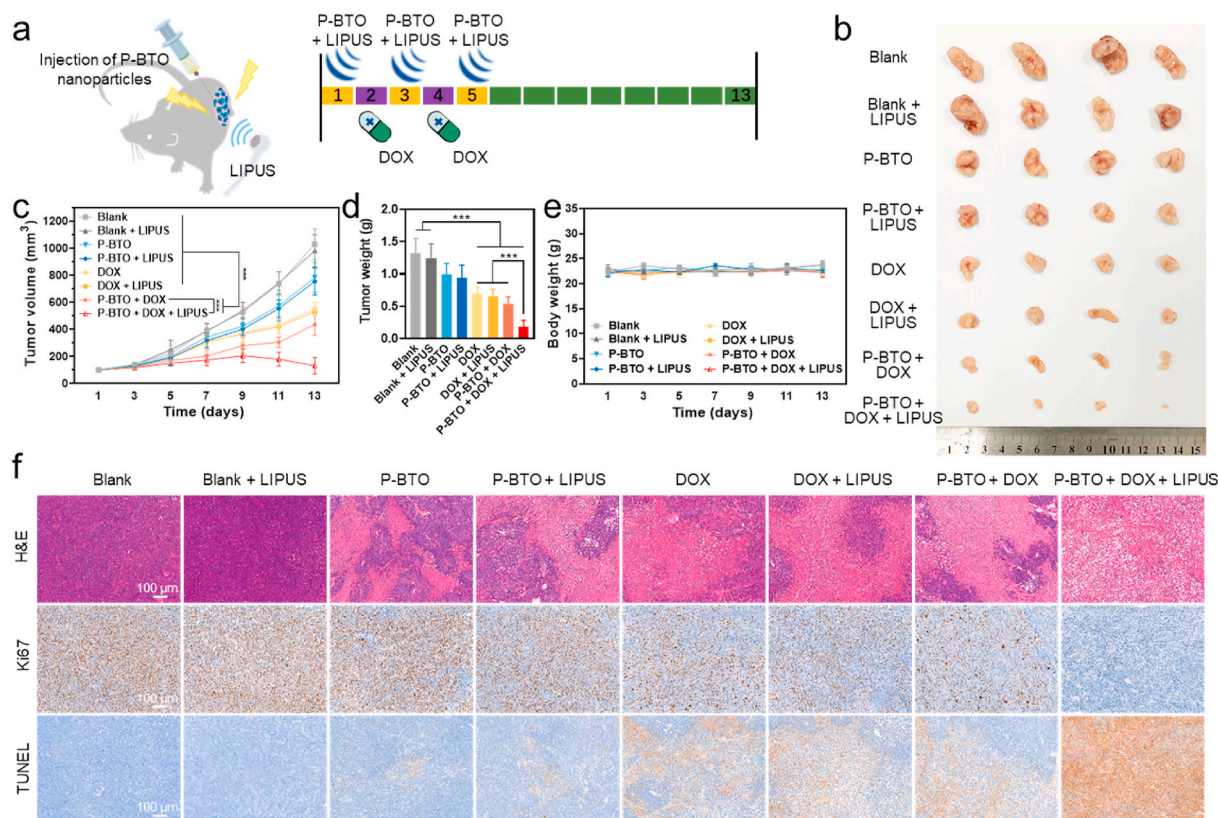


Fig. 5. Effect of wireless electrical stimulation on tumor chemotherapy *in vivo*. (a) Schematic diagram of the treatment plan of combined chemotherapy drugs. (b) Photographs of the tumors taken from the A375 tumor-bearing nude mice at the end of the antitumor studies. (c) Tumor volume. Data are mean \pm s.d. of biological replicates ($n = 6$). (d) Tumor weight. Data are mean \pm s.d. of biological replicates ($n = 6$). (e) Body weight. Data are mean \pm s.d. of biological replicates ($n = 6$). (f) H&E, Ki67 and TUNEL staining of tumor sections. * $p < 0.05$, ** $p < 0.01$ or *** $p < 0.001$. Tumor vascular normalization induced by wireless electrical stimulation could potentiate doxorubicin efficacy.

disappearance [58]. However, the local tumor tissue necrosis occurred in the P-BTO and P-BTO + LIPUS groups, which may be attributed to the surface electrostatic potential of nanoparticles inducing tumor cell apoptosis to a certain extent [59]. The expression of Ki-67 and the TUNEL assay also reflected the significantly inhibited tumor cell proliferation and the strongest apoptosis signal in the combined treatment group [60]. Additionally, histological examination of major organs also showed no significant pathological injury in any of the treatment groups for 13 days (Fig. S9). These data suggested that tumor vascular normalization induced by wireless electrical stimulation greatly potentiated the efficacy of DOX. Thus, on the premise of good biological safety, the application of wireless electrical stimulation in tumor-bearing mice is of great clinical value for the adjuvant treatment of malignant tumors.

Inspired by the role of endogenous bioelectricity in vessel formation, the wireless electrical stimulation therapeutic strategy was first proposed for tumor vascular normalization. This approach, based on piezoelectric nano-biomaterials, has cell-scale accuracy and high biocompatibility, which may circumvent the side effects of traditional anti-angiogenic drugs and solve the problem of the invasiveness of external electrical stimulation. Taking into account the characteristics of different tumor types, the magnitude and time of electrical stimulation can be adjusted by changing the ultrasound parameters within the safe range, which can achieve more precise and effective treatment in the future. Our ultimate goal is to create and maintain a functionally normal vasculature, which is healthier for cancer patients and can greatly accelerate the cancer treatment procedure.

3. Conclusion

In summary, we developed a wireless electrical stimulation therapeutic strategy for tumor vascular normalization based on piezoelectric nanoparticles. P-BTO nanoparticles with enhanced mechano-electrical conversion efficiency were prepared and their ability to generate wireless electrical stimulation at the nanoscale interface in response to LIPUS was proved. Our results indicated that wireless electrical stimulation was able to inhibit the migration and differentiation of endothelial cells by downregulating the eNOS/NO pathway, which may be caused by the destruction of the intracellular calcium ion gradient. Furthermore, animal experiments demonstrated that, with good biological safety, the normalized vascular structure and function achieved with this approach strengthened the efficacy of the chemotherapy drug. In general, this new type of wireless electrical stimulation system for non-invasive and efficient tumor vascular normalization has broad application prospects in the clinical auxiliary treatment of malignant tumors.

4. Materials and methods

4.1. Preparation of barium titanate nanoparticles

Barium titanate (BTO) nanoparticles were prepared based on a solvothermal process. Briefly, 8.509 g (25 mmol) titanium butoxide (99.0%, Aladdin, China) was dissolved in anhydrous ethanol, and then 5 mL ammonia solution (25% NH₃ in H₂O, Aladdin, China) was slowly added into the above solution and stirred for 15 min. 11.025 g (35 mmol) barium hydroxide octahydrate (98.0%, Macklin, China) was dissolved in 25 mL deionized water, and stirred in a 90°C-water bath until completely dissolved. The titanium butoxide solution mixture was then slowly added to the aqueous barium hydroxide octahydrate solution and stirred for 15 min, followed by a drop of 5 mL DEA (Aladdin, China) and continued stirring for 15 min. The final mixture was transferred to a 100 mL polytetrafluoroethylene liner in a hydrothermal reactor and incubated at 200 °C for 48 h. After the reaction, the resultant product was washed repeatedly using deionized water and ethanol and then dried at 60 °C for 24 h. Ultimately, BTO powder was loaded into an insulating mold with upper and lower copper sheets as polarized

electrodes, and then polarized by treating with a voltage of 2.5 kV for 30 min. The untreated BTO and polarized BTO nanoparticles were denoted as U-BTO and P-BTO.

4.2. Characterization of barium titanate nanoparticles

The morphology and structure of U-BTO and P-BTO nanoparticles were determined by high-resolution transmission electron microscopy (TEM, JEM-2100, JEOL, Japan) and field emission scanning electron microscopy (FE-SEM, Merlin, Carl Zeiss, Germany). Element distribution was measured by energy dispersive spectroscopy (EDS, OxFord instruments, UK) with an acceleration voltage of 20 kV. Crystallographic characterization was conducted via x-ray diffraction with monochromatic Cu K α radiation (XRD, D8 advance, Bruker, Germany) in the 2 θ range 5–60° with a step size of 0.02°. The molecular structure and component were observed by Raman spectrometer (Raman, LabRAM Aramis, HJY, France). The size was examined using a Zetasizer system (Zetasizer Nano ZS, Malvern Instruments, UK). Piezoresponse force microscopic (PFM) measurements were carried using an atomic force microscope (AFM, Bruker Multimode 8, Germany) with a Bruker AFM Probe (Co/Cr, 5.0 N/m, 150 kHz).

4.3. Low-intensity pulsed ultrasound stimulation (LIPUS)

An ultrasonic treatment instrument (HB810B, Haobro, China) was used in this study. The parameters used for stimulation were as follows: 1 MHz pulsed frequency and 1.0 W/cm² spatial average and temporal average incident intensity. During treatment, the transducer head was centered underneath the cell culture plates or on the skin of the tumor site, and coupling gel was carefully smeared to ensure the transmission of LIPUS. Devices were sterilized before use.

4.4. Finite element modeling (FEM) of piezoelectric potential distribution

To study the piezoelectric potential of U-BTO and P-BTO nanoparticles, FEM simulations with commercially available software COMSOL (5.3a, Burlington, USA) were performed. The simulation involved a dynamic 3D analysis using the piezoelectric device of multiphysics interface. The geometrical characteristics of BTO models were: 120 nm in width, 120 nm in length, and 120 nm in height. The middle of the model was fixed and grounded. To simulate the pressure generated by ultrasound, a mechanical field of 10⁸ Pa was applied to all surfaces [61].

4.5. Mechano-electrical response property

The mechano-electrical response property of BTO nanoparticles was evaluated by a Keithley universal digital meter (DMM7510, Keithley, USA). Specifically, we made a polytetrafluoroethylene mold (cylinder with diameter of 1 cm and height of 0.3 cm) for loading nanoparticles with two ends connected to the two poles of the digital meter to form a closed electrode. During the experiment, the equal mass of nanoparticle dry powder was filled into the mold, and the coupling gel was coated at the bottom of the negative electrode. Mechanical stimulation was applied through the ultrasound probe, and the real-time electrical signal output was collected at the monitoring frequency of 1/0.02 s. Finally, the voltage outputs of BTO nanoparticles under LIPUS instrument was exported through a wire and then recorded and saved by a computer.

4.6. Cell culture and in vitro cytotoxicity assay

Human umbilical vein endothelial cells (HUVECs, obtained from ScienCell Research Laboratories) were cultured in endothelial cell medium (ECM, ScienCell, USA) supplemented with 5% fetal bovine serum (FBS, ScienCell, USA), 1% endothelial cell growth supplement (ECGS, ScienCell, USA) and 1% penicillin/streptomycin solution (P/S,

ScienCell, USA). Human melanoma cell line (A375, obtained from the American Tissue Culture Collection), were cultured in Dulbecco's Modified Eagle's Medium (DMEM, high glucose, Gibco, USA) containing 10% fetal bovine serum (FBS, Gibco, USA) and 1% penicillin/streptomycin solution (P/S, Gibco, USA). All cell cultures were maintained at 37 °C in 5% CO₂ incubator, and the medium was changed every 2 days. HUVECs within passages 3 to 7 were used for experiments.

HUVECs were seeded in 96-well plates (5×10^3 cells/well) and co-cultured with various concentrations of BTO nanoparticles (0, 10, 25, 50, 100 and 200 µg/mL) for 24 h. Then, for the LIPUS treatment group, cells were treated with LIPUS for 1 min per day as described above. After culturing for another 24 h, the cell cytotoxicity was detected by Cell Counting KIT-8 (CCK-8, Dojindo, Japan) assay, and the optical density (OD) value at 450 nm was detected by a microplate reader (Cytation 5, BioTek, USA). Optimally, the concentration of BTO nanoparticles used in the subsequent *in vitro* experiments was 100 µg/mL.

4.7. Scratch wound assay

HUVECs were seeded in 6-well plates (5×10^5 cells/well) overnight. Once cells were confluent, the layer was scratched with a 20-µL pipette tip and was washed three times with Dulbecco's phosphate buffered saline (DPBS, Gibco, USA). The medium containing BTO nanoparticles was then added and treated with LIPUS for 1 min. Images were captured with an inverted fluorescence microscope at 0 and 24 h; then, the cell migration rate was analyzed with ImageJ software.

4.8. Tube formation assay

An *in vitro* angiogenesis assay was performed using Matrigel (ECMatrix™, Corning, USA). Briefly, 96-well plate was coated with Matrigel and then incubated at 37 °C for 1 h to allow solidification. Then, HUVECs (1×10^5 cells/well) with BTO nanoparticles were added and treated with LIPUS for 1 min. After culturing for 12 h, at least five random microscopic fields were photographed, using an inverted fluorescence microscope. The capillary tube branch number and tube length were analyzed with ImageJ software to quantify the angiogenesis process.

4.9. Cytoskeleton staining

F-actin cytoskeletal staining was performed using the fluorescent dye Actin-Tracker Green (Beyotime, China). HUVECs were seeded on confocal dish (NEST, China) at a density of 2×10^4 cells/well. Subsequently, BTO nanoparticles were added for incubation, during which LIPUS treatment (1 min) was performed twice. After culturing for 48 h, the cells were washed with PBS, and then fixed with 4% paraformaldehyde (Biosharp, China) for 10 min. After washed with PBS containing 0.1% Triton X-100 (Sigma Aldrich, USA), the samples were sequentially stained with Actin-Tracker Green (1:200 in PBS solution, 1 h) solution and 4',6-diamidino-2-phenylindole (3min; DAPI, Beyotime, China) solution for F-actin cytoskeleton and cell nucleus visualization respectively. Then the stained samples were observed by a confocal laser scanning microscope (CLSM, TCS SP8, Leica, Germany).

4.10. Intracellular nitric oxide measurement

Intracellular nitric oxide level was performed using the fluorescent probe 3-amino-4-(aminomethyl)-2',7'-difluorescein, diacetate (DAF-FM DA, Beyotime, China). HUVECs were seeded on confocal dish at a density of 2×10^4 cells/well. Subsequently, BTO nanoparticles were added for incubation, during which LIPUS treatment (1 min) was performed twice. After culturing for 48 h, the cells were washed with DPBS, and then incubated with 5 µmol/L DAF-FM DA for 30 min at 37 °C, in the dark. Fluorescence images were obtained by CLSM, and further quantitative analysis were performed using ImageJ software.

4.11. Intracellular calcium ion imaging

Intracellular calcium ion localization was performed using the fluorescent dye Fluo-4AM (Beyotime, China). HUVECs were seeded on a confocal dish at a density of 4×10^4 cells/well. After culturing for 24 h, the cells were washed with DPBS, and then incubated with 5 µmol/L Fluo-4AM in DPBS for 30 min at 37 °C in the dark. Subsequently, BTO nanoparticles were added and real-time calcium ion imaging was performed after LIPUS treatment (10 s) and captured by CLSM.

4.12. Membrane potential measurements

Cell membrane potential was measured using the fluorescence dye DiBAC4(3) (Dojindo, Japan). HUVECs were seeded on a confocal dish at a density of 4×10^4 cells/well. After culturing for 24 h, the cells were washed with DPBS, and then incubated with 5 µmol/L DiBAC4(3) diluted with 20 mmol/L 4-(2-hydroxyethyl)-1-piperazineethanesulfonic acid (HEPES, Sigma Aldrich, USA) for 30 min at 37 °C, in the dark. Subsequently, BTO nanoparticles were added and LIPUS treatment (10 s) was performed. Fluorescence images were obtained using CLSM.

4.13. Intracellular endocytosis assay

HUVECs were seeded on a confocal dish (NEST, China) at a density of 2×10^4 cells/well and incubated for 12 h at 37 °C. Then, the medium was replaced with fresh ECM containing fluorescein isothiocyanate (FITC)-labeled U-BTO/P-BTO, after which cells were cultured for 0, 3, and 6 h, respectively. The cells were stained with Actin-Tracker Red (30 min, Beyotime, China) and DAPI (3min) at 37 °C in the dark. Fluorescent images were captured using CLSM.

4.14. Quantitative real-time polymerase chain reaction

The expression of genes associated with angiogenesis was measured by quantitative real-time polymerase chain reaction (qRT-PCR). HUVECs were seeded in 48-well plates at a density of 2×10^4 cells/well. Then, BTO nanoparticles were added, and cells were incubated, while LIPUS treatment (1 min) was performed once per day. After culturing for 48 h, total RNA was extracted from samples using a HiPure Total RNA Kit (Magentec, China), and reverse transcribed into cDNA using a PrimeScript® RT reagent Kit (TaKaRa Biotechnology, Japan). Then, the RNA concentration was determined by spectrophotometry (Nanodrop 2000, Thermo Scientific, USA). A SYBR green dye (Invitrogen, USA) was used in qRT-PCR. Samples were held at 95 °C for 30 s, followed by 34 cycles at 95 °C for 5 s and 60 °C for 30 s. The sequences of primers for the *VEGF*, *FGF2*, *TGF-β1*, *NOS3* and *GAPDH* are given in Table S1. *GAPDH* was used as housekeeping gene for normalization. The $\Delta\Delta C_t$ -value method was used to analyze the relative changes.

4.15. Animal model and treatment protocol

All animal experiments were approved by Laboratory Animal Center of South China University of Technology. Female nude mice (6–8 weeks) were purchased from Hunan SJA Laboratory Animal Co., Ltd. Tumors were established by subcutaneous injection of A375 cells ($3 \times 10^6/100$ µL). The growth of tumors was evaluated by slide caliper and the tumor volume (V) was calculated as $\text{length} \times \text{width}^2/2$. The tumor volume and body weight of each mouse were determined every 2 days. Studies were carried out when the tumor volume reached 100–125 mm³.

For the assay of the tumor vessel structure to evaluate the tumor vascular normalization effect of the treatment, the mice were divided into six experimental groups randomly (n = 6): (1) blank (saline), (2) blank + LIPUS, (3) U-BTO, (4) U-BTO + LIPUS, (5) P-BTO, (6) P-BTO + LIPUS. Intratumoral nanoparticles injection (2.5 mg/kg) and LIPUS treatment (10 min) were performed every other day for a total of three times. Then, the mice were further processed to evaluate the vascular

normalization-related indicators.

To evaluate the combination of anti-tumor efficacy with chemotherapy drugs, the mice were divided into eight experimental groups randomly ($n = 6$): (1) blank (saline), (2) blank + LIPUS, (3) P-BTO, (4) P-BTO + LIPUS, (5) DOX, (6) DOX + LIPUS, (7) P-BTO + DOX, (8) P-BTO + DOX + LIPUS. Intratumoral nanoparticles injection (2.5 mg/kg) and LIPUS treatment (10 min) were performed every other day, three times in total. Intravenous DOX injection (3 mg/kg, Macklin, China) was interlaced with the time of nanoparticle treatment, and was also performed every other day, twice in total. The tumor volume and body weight of each mouse were monitored and recorded every 3 days. All the mice were sacrificed at Day 21. The tumor was excised and used for further analyses.

4.16. Vascular morphology

Tumors were captured and fixed in 4% paraformaldehyde for immunofluorescence studies. After dehydrating for 24 h, the tumor tissues were cut into slices with a thickness of 10 μm . To assess vascular density and pericyte coverage, slices stained with Anti-CD31 antibody (1:500, Abcam, USA) and α -SMA antibody (1:500, Abcam, USA). After gently washing twice with DPBS, tumor sections were incubated for 1 h at room temperature with secondary antibody conjugated to FITC or TRITC (1:100, Bioss, China). The nucleus was stained with DAPI. The fluorescence intensity was observed by CLSM. Pericyte coverage was quantified using the Colocalization plug-in of ImageJ software.

4.17. Tumor vascular leakage and perfusion assay

To assess vascular leakage, mice were intravenously injected with TRITC-Dextran (40 kDa, 10 mg/kg, GlycoSci, China). After 1 h, FITC-Lectin (1 mg/kg, Sigma, USA) was injected to analyze tumor vessel perfusion. After 10 min, animals were sacrificed and the tumor tissues were harvested, embedded in optimal cutting temperature compound medium, and cut into cryosections. Sections were fixed in 4% paraformaldehyde, stained with DAPI. Finally, images were acquired from five non-repeating fields of view using CLSM.

4.18. Hypoxia detection by pimonidazole

For tumor hypoxia studies, pimonidazole (60 mg/kg, Hypoxyprobe, Burlington, USA) was intraperitoneally injected 1 h before sacrifice. Samples were fixed with 4% paraformaldehyde. The detection and location of cells undergoing hypoxia were determined using anti-pimonidazole immunohistochemical staining. The sections were photographed using a microscope (Zeiss, Germany).

4.19. Histopathology and immunohistochemical analysis

To assess the anti-tumor effect and biological safety, tumor and major organs (heart, liver, spleen, lungs, and kidneys) collected from tumor-bearing mice were harvested and fixed in 4% paraformaldehyde. These tissues were embedded in paraffin and cut into 10- μm sections and stained with hematoxylin and eosin (H&E). For Ki67 staining, tumor sections were stained with Anti-Ki67 antibody (1: 500, Servicebio, China). Then, they were washed twice with DPBS, and incubated with horseradish peroxidase-conjugated secondary antibody respectively for 1h (1:3000, Servicebio, USA). For terminal deoxynucleotidyl transferase-mediated deoxyuridine triphosphate nick-end labeling (TUNEL) staining, tumor sections were incubated with 0.3% H_2O_2 in distilled water for 5 min at room temperature and then were performed using the ApopTag Peroxidase In Situ Apoptosis Detection kit (Merck Millipore, USA) in accordance with the manufacturer's instructions. These sections were photographed using a microscope (Zeiss, Germany).

4.20. Statistical analyses

Data were presented as mean \pm standard deviation (SD). Student's *t*-test and one-way analysis of variance with a multiple comparisons test were carried out, and values of $*p < 0.05$ were considered to be statistically significant.

CRediT authorship contribution statement

Changhao Li: Conceptualization, Data curation, Formal analysis, Investigation, Writing – original draft, Methodology. **Cairong Xiao:** Conceptualization, Investigation, Methodology, Validation. **Lizhen Zhan:** Investigation, Methodology, Validation. **Zhekun Zhang:** Investigation, Methodology, Validation. **Jun Xing:** Conceptualization, Formal analysis. **Jinxia Zhai:** Conceptualization, Formal analysis. **Zhengnan Zhou:** Conceptualization, Formal analysis. **Guoxin Tan:** Conceptualization. **Jinhua Piao:** Funding acquisition. **Yahong Zhou:** Conceptualization, Supervision. **Suijian Qi:** Conceptualization, Validation, Writing – review & editing. **Zhengao Wang:** Funding acquisition, Supervision. **Peng Yu:** Conceptualization, Validation, Funding acquisition, Writing – review & editing. **Chengyun Ning:** Conceptualization, Funding acquisition, Supervision.

Declaration of competing interest

All authors declare that they have no conflicts of interest and no competing interest.

Acknowledgements

This work is financially supported by the National Natural Science Foundation of China (Nos. 51932002, 52072127, 51903087, 52003085, 21975079), the Science and Technology Program of Guangzhou (No. 202002030308).

Appendix A. Supplementary data

Supplementary data to this article can be found online at <https://doi.org/10.1016/j.bioactmat.2022.03.027>.

References

- [1] A.M.E. Abdalla, L. Xiao, M.W. Ullah, M. Yu, C. Ouyang, G. Yang, Current challenges of cancer anti-angiogenic therapy and the promise of nanotherapeutics, *Theranostics* 8 (2018) 533–548.
- [2] M.W. Dewhirst, T.W. Secomb, Transport of drugs from blood vessels to tumour tissue, *Nat. Rev. Cancer* 17 (2017) 738–750.
- [3] R.K. Jain, Normalization of tumor vasculature: an emerging concept in antiangiogenic therapy, *Science* 307 (2005) 58–62.
- [4] C. Viillard, B. Larrivee, Tumor angiogenesis and vascular normalization: alternative therapeutic targets, *Angiogenesis* 20 (2017) 409–426.
- [5] G. Bergers, D. Hanahan, Modes of resistance to anti-angiogenic therapy, *Nat. Rev. Cancer* 8 (2008) 592–603.
- [6] G.C. Jayson, R. Kerbel, L.M. Ellis, A.L. Harris, Antiangiogenic therapy in oncology: current status and future directions, *Lancet* 388 (2016) 518–529.
- [7] D. Ribatti, A.G. Solimando, F. Pezzella, The Anti-VEGF(R) drug discovery legacy: improving attrition rates by breaking the vicious cycle of angiogenesis in cancer, *Cancers* 13 (2021) 3433.
- [8] S. Du, H. Xiong, C. Xu, Y. Lu, J. Yao, Attempts to strengthen and simplify the tumor vascular normalization strategy using tumor vessel normalization promoting nanomedicines, *Biomater. Sci.* 7 (2019) 1147–1160.
- [9] F. Mpekris, C. Voutouri, J.W. Baish, D.G. Duda, L.L. Munn, T. Stylianopoulos, R. K. Jain, Combining microenvironment normalization strategies to improve cancer immunotherapy, *Proc. Natl. Acad. Sci. U.S.A.* 117 (2020) 3728–3737.
- [10] M. Levin, Molecular bioelectricity: how endogenous voltage potentials control cell behavior and instruct pattern regulation in vivo, *Mol. Biol. Cell* 25 (2014) 3835–3850.
- [11] P.L. Farber, F.C. Isoldi, L.M. Ferreira, Electric factors in wound healing, *Adv. Wound Care* 10 (2021) 461–476.
- [12] H. Fukui, R.W. Chow, J. Xie, Y.Y. Foo, C.H. Yap, N. Minc, N. Mochizuki, J. Vermot, Bioelectric signaling and the control of cardiac cell identity in response to mechanical forces, *Science* 374 (2021) 351–354.

- [13] P. Zhou, F. He, Y. Han, B. Liu, S. Wei, Nanosecond pulsed electric field induces calcium mobilization in osteoblasts, *Bioelectrochemistry* 124 (2018) 7–12.
- [14] P.M. Graybill, A. Jana, R.K. Kapania, A.S. Nain, R.V. Davalos, Single cell forces after electroporation, *ACS Nano* 15 (2021) 2554–2568.
- [15] G. Thrivikraman, S.K. Boda, B. Basu, Unraveling the mechanistic effects of electric field stimulation towards directing stem cell fate and function: a tissue engineering perspective, *Biomaterials* 150 (2018) 60–86.
- [16] R. Nuccitelli, X. Chen, A.G. Pakhomov, W.H. Baldwin, S. Sheikh, J.L. Pomier, W. Ren, C. Osgood, R.J. Swanson, J.F. Kolb, S.J. Beebe, K.H. Schoenbach, A new pulsed electric field therapy for melanoma disrupts the tumor's blood supply and causes complete remission without recurrence, *Int. J. Cancer* 125 (2009) 438–445.
- [17] X. Chen, J.F. Kolb, R.J. Swanson, K.H. Schoenbach, S.J. Beebe, Apoptosis initiation and angiogenesis inhibition: melanoma targets for nanosecond pulsed electric fields, *Pigm. Cell Melanoma Res.* 23 (2010) 554–563.
- [18] L. Wu, C. Yao, Z. Xiong, R. Zhang, Z. Wang, Y. Wu, Q. Qin, Y. Hua, The effects of a picosecond pulsed electric field on angiogenesis in the cervical cancer xenograft models, *Gynecol. Oncol.* 141 (2016) 175–181.
- [19] S. Wu, Y. Wang, J. Guo, Q. Chen, J. Zhang, J. Fang, Nanosecond pulsed electric fields as a novel drug free therapy for breast cancer: an in vivo study, *Cancer Lett* 343 (2014) 268–274.
- [20] R. Nuccitelli, Application of pulsed electric fields to cancer therapy, *Bioelectricity* 1 (2019) 30–34.
- [21] D. Miklavcic, V. Novickij, M. Kranjc, T. Polajzer, S. Haberl Meglic, T. Batista Napotnik, R. Romih, D. Lisjak, Contactless electroporation induced by high intensity pulsed electromagnetic fields via distributed nanoelectrodes, *Bioelectrochemistry* 132 (2020), 107440.
- [22] K. Kapat, Q.T.H. Shubhra, M. Zhou, S. Leeuwenburgh, Piezoelectric nanomaterials for biomedicine and tissue regeneration, *Adv. Funct. Mater.* 30 (2020), 1909045.
- [23] K. Cai, Y. Jiao, Q. Quan, Y. Hao, J. Liu, L. Wu, Improved activity of MC3T3-E1 cells by the exciting piezoelectric BaTiO₃/TC4 using low-intensity pulsed ultrasound, *Bioact. Mater.* 6 (2021) 4073–4082.
- [24] A. Cafarelli, A. Marino, L. Vannozi, J. Puigmarti-Luis, S. Pane, G. Ciofani, L. Ricotti, Piezoelectric nanomaterials activated by ultrasound: the pathway from discovery to future clinical adoption, *ACS Nano* 15 (2021) 11066–11086.
- [25] C.-H. Hong, H.-P. Kim, B.-Y. Choi, H.-S. Han, J.S. Son, C.W. Ahn, W. Jo, Lead-free piezoceramics – where to move on? *J. Materomics* 2 (2016) 1–24.
- [26] D. Hu, H. Ma, Y. Tanaka, L. Zhao, Q. Feng, Ferroelectric mesocrystalline BaTiO₃/SrTiO₃ nanocomposites with enhanced dielectric and piezoelectric responses, *Chem. Mater.* 27 (2015) 4983–4994.
- [27] V. Bansal, P. Poddar, A. Ahmad, M. Sastry, Room-temperature biosynthesis of ferroelectric barium titanate nanoparticles, *J. Am. Chem. Soc.* 128 (2006) 11958–11963.
- [28] N. Lv, W.B. Jiang, K.S. Hu, Z.W. Lyu, Synchronous construction of piezoelectric elements and nanoresistance networks for pressure sensing based on the wheatstone bridge principle, *ACS Appl. Electron. Mater.* 3 (2021) 3936–3947.
- [29] L. Zhao, Y. Zhang, F. Wang, S. Hu, X. Wang, B. Ma, H. Liu, Z. Wang, Y. Sang, BaTiO₃ nanocrystal-mediated micro pseudo-electrochemical cells with ultrasound-driven piezotronic enhancement for polymerization, *Nano Energy* 39 (2017) 461–469.
- [30] G. Canavese, A. Ancona, L. Racca, M. Canta, B. Dumontel, F. Barbaresco, T. Limongi, V. Cauda, Nanoparticle-assisted ultrasound: a special focus on sonodynamic therapy against cancer, *Chem. Eng. J.* 340 (2018) 155–172.
- [31] V.K. Kallianagounder, N.P.M.J. Raj, A.R. Unnithan, J. Park, S.S. Park, S.J. Kim, C. H. Park, C.S. Kim, A.R.K. Sasikala, Remotely controlled self-powering electrical stimulators for osteogenic differentiation using bone inspired bioactive piezoelectric whitlockite nanoparticles, *Nano Energy* 85 (2021), 105901.
- [32] J. Cao, M. Ehling, S. Marz, J. Seebach, K. Tarbashevich, T. Sixta, M.E. Pitulescu, A. C. Werner, B. Flach, E. Montanez, E. Raz, R.H. Adams, H. Schnittler, Polarized actin and VE-cadherin dynamics regulate junctional remodelling and cell migration during sprouting angiogenesis, *Nat. Commun.* 8 (2017) 2210.
- [33] J. Cho, S. Kim, H. Lee, W. Rah, H.C. Cho, N.K. Kim, S. Bae, D.H. Shin, M.G. Lee, I. H. Park, Y. Tanaka, E. Shin, H. Yi, J.W. Han, P.T.J. Hwang, H.W. Jun, H.J. Park, K. Cho, S.W. Lee, J.K. Jung, R.D. Levit, M.A. Sussman, R.P. Harvey, Y.S. Yoon, Regeneration of infarcted mouse hearts by cardiovascular tissue formed via the direct reprogramming of mouse fibroblasts, *Nat. Biomed. Eng.* 5 (2021) 880–896.
- [34] O. Sen, A. Marino, C. Pucci, G. Ciofani, Modulation of anti-angiogenic activity using ultrasound-activated nutlin-loaded piezoelectric nanovectors, *Mater. Today Bio* 13 (2022), 100196.
- [35] S. Tojkander, G. Gateva, P. Lappalainen, Actin stress fibers – assembly, dynamics and biological roles, *J. Cell Sci.* 125 (2012) 1855–1864.
- [36] C. Pucci, A. Marino, O. Sen, D. De Pasquale, M. Bartolucci, N. Iturriz-Rodriguez, N. di Leo, G. de Vito, D. Debellis, A. Petretto, G. Ciofani, Ultrasound-responsive nutlin-loaded nanoparticles for combined chemotherapy and piezoelectric treatment of glioblastoma cells, *Acta Biomater* 139 (2022) 218–236.
- [37] Y. Tian, F. Zhang, Y. Qiu, S. Wang, F. Li, J. Zhao, C. Pan, Y. Tao, D. Yu, W. Wei, Reduction of choroidal neovascularization via cleavable VEGF antibodies conjugated to exosomes derived from regulatory T cells, *Nat. Biomed. Eng.* 5 (2021) 968–982.
- [38] M.K. Priya, G. Sahu, D.R. Soto-Pantoja, N. Goldy, A.M. Sundaresan, V. Jadhav, T. R. Barathkumar, U. Saran, B.M. Jaffar Ali, D.D. Roberts, A.K. Bera, S. Chatterjee, Tipping off endothelial tubes: nitric oxide drives tip cells, *Angiogenesis* 18 (2015) 175–189.
- [39] V. Garcia, W.C. Sessa, Endothelial NOS: perspective and recent developments, *Br. J. Pharmacol.* 176 (2019) 189–196.
- [40] P.-M. Yang, Y.-T. Huang, Y.-Q. Zhang, C.-W. Hsieh, B.-S. Wung, Carbon monoxide releasing molecule induces endothelial nitric oxide synthase activation through a calcium and phosphatidylinositol 3-kinase/Akt mechanism, *Vasc. Pharmacol.* 87 (2016) 209–218.
- [41] C. Mattheus, X. Lian, S. Kunz, M. Lehmann, C. Zhong, C. Bernert, I. Lahmann, D. N. Muller, M. Gollasch, O. Daumke, eNOS-NO-induced small blood vessel relaxation requires EHD2-dependent caveolae stabilization, *PLoS One* 14 (2019), e0223620.
- [42] Y. Hu, M. Chen, M. Wang, X. Li, Flow-mediated vasodilation through mechanosensitive G protein-coupled receptors in endothelial cells, *Trends Cardiovasc. Med.* 21 (2021) S1050–S1738.
- [43] Y. Li, W.K. Yu, L. Chen, Y.S. Chan, D. Liu, C.C. Fong, T. Xu, G. Zhu, D. Sun, M. Yang, Electrotaxis of tumor-initiating cells of H1975 lung adenocarcinoma cells is associated with both activation of stretch-activated cation channels (SACCs) and internal calcium release, *Bioelectrochemistry* 124 (2018) 80–92.
- [44] R.A. Brundage, K.E. Fogarty, R.A. Tuft, F.S. Fay, Calcium gradients underlying polarization and chemotaxis of eosinophils, *Science* 254 (1991) 703–706.
- [45] T.T. Liu, X.F. Du, B.B. Zhang, H.X. Zi, Y. Yan, J.A. Yin, H. Hou, S.Y. Gu, Q. Chen, J. L. Du, Piezo1-mediated Ca(2+) activities regulate brain vascular pathfinding during development, *Neuron* 108 (2020) 180–192.
- [46] X. Huang, J. Xing, Z.G. Wang, J. Han, R.X. Wang, C.H. Li, C.R. Xiao, F. Lu, J. X. Zhai, Z.N. Zhou, Y.F. Li, L. Zhou, Z.G. Song, D.F. Chen, P. Yu, C.Y. Ning, X. Y. Jiang, OD/1D heterojunction implant with electro-mechanobiological coupling cues promotes osteogenesis, *Adv. Funct. Mater.* 31 (2021), 2106249.
- [47] I. Golovynska, S. Golovynskiy, Y.V. Stepanov, L.I. Stepanova, J. Qu, T. Y. Ohulchanskyy, Red and near-infrared light evokes Ca(2+) influx, endoplasmic reticulum release and membrane depolarization in neurons and cancer cells, *J. Photochem. Photobiol., B* 214 (2021) 112088.
- [48] F. Moccia, S. Negri, M. Shekha, P. Paris, G. Guerra, Endothelial Ca(2+) signaling, angiogenesis and vasculogenesis: just what it takes to make a blood vessel, *Int. J. Mol. Sci.* 20 (2019) 3962.
- [49] A.M. Savage, S. Kurusamy, Y. Chen, Z. Jiang, K. Chhabria, R.B. MacDonald, H. R. Kim, H.L. Wilson, F.J.M. van Eeden, A.L. Armesilla, T.J.A. Chico, R. N. Wilkinson, tmem33 is essential for VEGF-mediated endothelial calcium oscillations and angiogenesis, *Nat. Commun.* 10 (2019) 732.
- [50] T. Liu, X. Du, B. Zhang, H. Zi, Y. Yan, J. Yin, H. Hou, S. Gu, Q. Chen, J. Du, Piezo1-mediated Ca(2+) activities regulate brain vascular pathfinding during development, *Neuron* 108 (2020) 180–192, e185.
- [51] Z. Jiang, H. Xiong, S. Yang, Y. Lu, Y. Deng, J. Yao, J. Yao, Jet-lagged nanoparticles enhanced immunotherapy efficiency through synergistic reconstruction of tumor microenvironment and normalized tumor vasculature, *Adv. Healthc. Mater.* 9 (2020), e2000075.
- [52] X. Zhang, K. Yang, C. Chen, Z. He, Q. Wang, H. Feng, S. Lv, Y. Wang, M. Mao, Q. Liu, Y. Tan, W. Wang, T. Li, L. Che, Z. Qin, L. Wu, M. Luo, C. Luo, Y. Liu, W. Yin, C. Wang, H. Guo, Q. Li, B. Wang, W. Chen, S. Wang, Y. Shi, X. Bian, Y. Ping, Pericytes augment glioblastoma cell resistance to temozolomide through CCL5-CCR5 paracrine signaling, *Cell Res* 31 (2021) 1072–1087.
- [53] T. Lv, Z. Li, L. Xu, Y. Zhang, H. Chen, Y. Gao, Chloroquine in combination with aptamer-modified nanocomplexes for tumor vessel normalization and efficient erlotinib/Survivin shRNA co-delivery to overcome drug resistance in EGFR-mutated non-small cell lung cancer, *Acta Biomater* 76 (2018) 257–274.
- [54] H.G. Song, A. Lammers, S. Sundaram, L. Rubio, A.X. Chen, L. Li, J. Eyckmans, S. N. Bhatia, C.S. Chen, Transient support from fibroblasts is sufficient to drive functional vascularization in engineered tissues, *Adv. Funct. Mater.* 30 (2020), 2003777.
- [55] D. Keskin, J. Kim, V.G. Cooke, C.C. Wu, H. Sugimoto, C. Gu, M. De Palma, R. Kalluri, V.S. LeBleu, Targeting vascular pericytes in hypoxic tumors increases lung metastasis via angiopoietin-2, *Cell Rep* 10 (2015) 1066–1081.
- [56] X. Xu, M. Chen, X. Lou, Y. Du, G. Shu, J. Qi, M. Zhu, X. Ying, L. Yu, J. Ji, Y. Du, Sialic acid-modified mesoporous polydopamine induces tumor vessel normalization to enhance photodynamic therapy by inhibiting VE-cadherin internalization, *Chem. Eng. J.* 414 (2021), 128743.
- [57] L. Pang, R. Zhao, J. Chen, J. Ding, X. Chen, W. Chai, X. Cui, X. Li, D. Wang, H. Pan, Osteogenic and anti-tumor Cu and Mn-doped borosilicate nanoparticles for synthetic bone repair and chemodynamic therapy in bone tumor treatment, *Bioact. Mater.* 12 (2022) 1–15.
- [58] Y. Guo, Y. Hu, X. Zheng, X. Cao, Q. Li, Z. Wei, Z. Zhu, S. Zhang, Self-assembled peptide nanoparticles with endosome escaping permits for co-drug delivery, *Talanta* 221 (2021) 121572.
- [59] C. Li, Y. Li, T. Yao, L. Zhou, C. Xiao, Z. Wang, J. Zhai, J. Xing, J. Chen, G. Tan, Y. Zhou, S. Qi, P. Yu, C. Ning, Wireless electrochemotherapy by selenium-doped piezoelectric biomaterials to enhance cancer cell apoptosis, *ACS Appl. Mater. Interfaces* 12 (2020) 34505–34513.
- [60] K. Matsumoto, T. Noda, S. Kobayashi, Y. Sakano, Y. Yokota, Y. Iwagami, D. Yamada, Y. Tomimaru, H. Akita, K. Gotoh, Y. Takeda, M. Tanemura, K. Umeshita, Y. Doki, H. Eguchi, Inhibition of glycolytic activator PFKFB3 suppresses tumor growth and induces tumor vessel normalization in hepatocellular carcinoma, *Cancer Lett* 500 (2021) 29–40.
- [61] J. Wu, N. Qin, D.H. Bao, Effective enhancement of piezocatalytic activity of BaTiO₃ nanowires under ultrasonic vibration, *Nano Energy* 45 (2018) 44–51.